POLITECNICO DI TORINO
Repository ISTITUZIONALE

Energy-efficient design and optimization of hollow fiber direct contact membrane distillation modules with integrated heat recovery

Original
Energy-efficient design and optimization of hollow fiber direct contact membrane distillation modules with integrated heat recovery / Sulaiman, H.F., Díaz-Quezada, S., Tabasian, A.N., Tiraferri, A., Quist-Jensen, C.A., Ali, A.. - In: JOURNAL OF WATER PROCESS ENGINEERING. - ISSN 2214-7144. - 92:(2026). [10.1016/j.jwpe.2026.110673]

Availability:
This version is available at: 11583/3014790 since: 2026-08-24T07:52:05Z

Publisher:
Elsevier

Published
DOI:10.1016/j.jwpe.2026.110673

Terms of use:

This article is made available under terms and conditions as specified in the corresponding bibliographic description in the repository

Publisher copyright

(Article begins on next page)

15 November 2026

Journal of Water Process Engineering 92 (2026) 110673

Contents lists available at ScienceDirect

Journal of Water Process Engineering

journal homepage: www.elsevier.com/locate/jwpe

Energy-efficient design and optimization of hollow fiber direct contact membrane distillation modules with integrated heat recovery

Hussein Fairousha Sulaiman [a], Simón Díaz-Quezada [a], Ali Naeimi Tabasian [b,c], Alberto Tiraferri [b,c], Cejna Anna Quist-Jensen [a], Aamer Ali [d,*]

[a] Center for Membrane Technology, Department of Chemistry and Bioscience, Aalborg University, Fredrik Bajers Vej 7H, 9220, Aalborg East, Denmark
[b] Department of Environment, Land and Infrastructure Engineering (DIATI), Politecnico di Torino, Corso Duca degli Abruzzi 24, 10129, Torino, Italy
[c] Clean Water Center, Politecnico di Torino, Corso Duca degli Abruzzi 24, 10129, Torino, Italy
[d] AAU Energy, Aalborg University, Pontoppidanstræde 111, 9220, Aalborg East, Denmark

ARTICLE INFO

Editor: Mingmei Ding

Keywords:
Direct Contact Membrane Distillation (DCMD)
Hollow fiber module design
Energy recovery strategy
Multi-objective optimization
Specific Thermal Energy Consumption (STEC)

ABSTRACT

Membrane distillation (MD) is a promising technology for sustainable freshwater production. Among its configurations, direct contact membrane distillation (DCMD) is attractive because of its simplicity, but large-scale deployment remains limited by high thermal energy demand. To address this challenge, this study presents an integrated framework for the design and optimization of hollow fiber DCMD modules with heat recovery under operational uncertainty. The novelty of this work lies in combining rigorous model validation with simultaneous optimization of module geometry and operating conditions to reduce net specific thermal energy consumption (STEC) while maintaining competitive permeate flux. A mechanistic model based on coupled mass and energy balances was validated against 26 experiments using lab-made and commercial hollow fiber modules without model-specific calibration. Excellent agreement was obtained, with coefficients of determination (R^2) of 0.96 for flux, 0.99 for feed outlet temperature, and 0.97 for permeate outlet temperature. Multi-objective optimization identified an optimal trade-off design with module length of 1.25 m and packing density of 0.75. Under optimized operating conditions, this design achieved an average flux of 4.5 kg m^{-2} h^{-1} at a net STEC of 205 kWh m^{-3}. Energy-focused operation reduced net STEC to 100 kWh m^{-3} at 2.2 kg m^{-2} h^{-1}, while high-productivity operation reached 5.5 kg m^{-2} h^{-1} at 630 kWh m^{-3}. Overall, the results show that validated model-based optimization of both module geometry and operation can substantially improve DCMD energy efficiency while preserving its structural simplicity and scalability.

1. Introduction

Demand for freshwater has increased significantly worldwide due to population growth, industrialization, and improved living standards. To bridge the growing gap between freshwater demand and supply, seawater desalination has become an essential technological solution. However, conventional desalination processes, such as reverse osmosis and multi-stage flash distillation, are energy intensive, relying heavily on high-grade energy sources (electricity or fossil fuels), and often exhibit limited freshwater recovery factors. Consequently, current research efforts in water treatment increasingly focus on the development of desalination technologies that are more energy -efficient, environmentally sustainable, and compatible with low-grade- heat sources [1].

Among emerging desalination processes, membrane distillation (MD) has attracted considerable attention due to its ability to utilize low-grade thermal energy and its suitability for treating highly concentrated brines [2,3]. MD uses a porous hydrophobic membrane to retain a warm liquid feed while allowing the passage of water vapor through the pores. The heat input can be supplied through different sources including solar, geothermal or industrial sources. The process typically operates at atmospheric pressure that results in minimum electric energy input to drive the liquid within the channels. MD can be operated in different configurations including direct contact, vacuum, air gap and sweep gap. Within MD configurations, direct contact membrane distillation (DCMD) stands out as the simplest to implement and the most straightforward to scale up, since it avoids the need for vacuum systems, additional condensers, or gas phase handling [3]. This

* Corresponding author.
E-mail address: aal@energy.aau.dk (A. Ali).

https://doi.org/10.1016/j.jwpe.2026.110673
Received 27 May 2026; Received in revised form 12 July 2026; Accepted 27 July 2026
Available online 3 August 2026
2214-7144/© 2026 The Authors. Published by Elsevier Ltd. This is an open access article under the CC BY license (http://creativecommons.org/licenses/by/4.0/).

simplicity makes DCMD particularly attractive for industrial-scale deployment.

Despite these advantages, DCMD faces a key challenge of high specific thermal energy consumption (STEC) that directly impacts its operational cost and hinders its broader adoption [4]. To improve the thermal energy efficiency of DCMD, several strategies have been adopted in the literature. These include module design modifications, such as optimization of flow channel geometry and spacers to enhance heat and mass transfer while mitigating temperature polarization [5], as well as membrane material optimization, for example by reducing membrane thickness or tuning thermal conductivity to minimize conductive heat losses [6]. In parallel, heat recovery has emerged as a particularly effective approach, in which thermal energy from the warm distillate stream is reused to preheat the feed stream, thereby reducing the net external energy demand of the process [7]. Heat recovery performance has been improved either by optimizing operating conditions (e.g., inlet temperatures and flow velocities) or by tuning key module design parameters, most notably the contact length between feed and permeate streams [8]. The key focus of the latter has been on optimizing the contact length of feed and permeate stream of DCMD under different operating conditions [9]. The desired contact length can be achieved by connecting modules in series or through innovative designs such as multipass hollow fiber modules [5,10]. In our previous studies, we have demonstrated that the specific thermal energy consumption of DCMD can be reduced significantly through optimization of the contact length and by choosing suitable operative conditions [5].

In addition to contact length, packing density is a critical module design parameter that governs the balance between module productivity and hydrodynamic performance, particularly on the shell side of hollow fiber modules. Packing density affects the available flow cross section, residence time, membrane area per module volume, and the relative distribution of feed and permeate flow rates. These factors strongly influence local temperature profiles, heat and mass transfer, and consequently the heat recovery potential and net specific thermal energy consumption (STEC) of DCMD systems. Although the effects of module length, packing density, and operating conditions on DCMD performance have each been examined individually in previous numerical and experimental studies [8,9,11], these variables have generally been investigated in isolation or through one-factor-at-a-time parametric analyses. For example, Cheng et al. [12] examined the influence of fiber length, packing density, and selected operating variables on productivity and thermal efficiency in hollow fiber DCMD, and demonstrated the trade-off between flux and thermal efficiency through Pareto optimization. Likewise, Yang et al. [13] investigated several novel hollow fiber module configurations, including curly, spacer-wrapped, and spacer-knitted fibers, and showed that improved hydrodynamics and reduced temperature polarization can substantially enhance permeate flux. These studies provide valuable insights into the effects of module geometry and flow behavior on DCMD performance. However, they generally focus on individual design parameters, fixed module configurations, or hydrodynamic enhancement, rather than on the coupled interactions between module geometry, operating conditions, and heat recovery. As a result, the simultaneous influence of module length, packing density, and operating conditions on heat recovery and net STEC remains insufficiently understood, particularly for hollow fiber DCMD modules.

Although significant reductions in STEC have been reported through optimization of individual operating conditions or isolated design parameters, most existing studies treat process optimization and module design separately. Extensive modeling efforts have been devoted to describing DCMD transport phenomena and guiding design improvements [2,14]; many available DCMD models rely on empirical fitting or case-specific calibration, which can restrict their predictive capability when transferred across different module configurations and operating windows. Therefore, a key knowledge gap remains in the development of a predictive and computationally efficient framework that can (i) accurately describe DCMD performance with heat recovery across different hollow fiber modules, (ii) jointly optimize module geometry and operating conditions, and (iii) account for the performance trade-offs between water productivity and thermal energy consumption under operational variability.

The present work addresses this gap by introducing an integrated modeling and optimization framework for hollow fiber DCMD with heat recovery. The novelty of the study is not the isolated investigation of module length or packing density themselves, but the combination of three elements within a single design-oriented framework: (i) a mechanistic DCMD model with explicit heat-recovery representation that is validated against experimental measurements from both lab-made and commercial hollow fiber modules without model-specific parameter fitting; (ii) a systematic analysis of the coupled effects of module length, packing density, feed/permeate temperatures, and flow velocities on flux and net STEC; and (iii) a multi-objective optimization strategy that simultaneously determines favorable module geometry and operating conditions while considering operational variability. By linking model validation, design optimization, and heat-recovery analysis in a unified framework, this work provides a more general methodology for identifying energy-efficient and manufacturable DCMD module designs than conventional parametric studies based on fixed designs or fixed operating conditions.

The paper is structured as follows: Section 2 presents the model formulation, numerical solution, and optimization procedure. Section 3 discusses the results of the validation, then the parametric study and optimization analysis. Finally, Section 4 summarizes the main conclusions and outlines perspectives for future research.

2. Methodology

This section describes the methodological framework adopted in this study. First, the proposed model is validated against experimental data to ensure its reliability. Then, the governing equations for heat and mass transfer, their one-dimensional balances, and the numerical solution strategy are presented. Finally, the optimization procedure is introduced, including the definition of decision variables, operational variability, and performance indicators.

For the sake of simplicity, the study is restricted to water as the working fluid. This methodological choice enables a comprehensive assessment of the fundamental transport mechanisms without the added complexity of solute effects, which have already been extensively studied in the context of concentration polarization [16].

2.1. Experimental validation

To generate *data* for model validation, four types of polypropylene hollow fiber membrane modules were used in the experiments, as shown in Fig. S1 in Supplementary Material. Modules 1 and 2 were fabricated in our laboratory whereas Module 3 was purchased from MANN+HUMMEL, Germany. Module type 4 consists of two Modules 3 connected in series.

The key geometrical features of the modules and main characteristics of the membrane used in their manufacturing are described in Table 1.

Several experiments were conducted to evaluate model accuracy. Table S1 in Supplementary Material presents data for validating the DCMD model. It includes 26 experiments conducted under various operating conditions. Experiments 1–9 were conducted with Membrane Module 1 and Experiments 10–18 used Membrane Module 2. Experiments 19–24 conducted with Membrane Module 3, while Experiments 25–26 used Membrane Module type 4 and were used to validate the prediction of the optimization framework. These conditions allow for a comprehensive evaluation of the model's predictive accuracy. Model validation involves simulating DCMD performance under these configurations and comparing predicted flux and outlet temperatures values with the experimental data.

Table 1
Characteristics of membrane and membrane modules used in experiments.

Characteristic	Membrane Module 1	Membrane Module 2	Membrane Module 3	Membrane Module 4
Number of fibers (n_{fibres})	10	25	40	40
Contact length (L)	0.51 m	0.51 m	0.5 m	1 m
Packing density (ϕ)	18%	46%	73%	73%
Membrane area (A_m)	0.04 m^2	0.09 m^2	0.14 m^2	0.28 m^2
Material	Polypropylene (PP)			
Pore size (d_p)	0.2 μm			
Porosity (ε)	73%			
Thermal Conductivity ($K_{polymer}$)	0.22 W/mK			
Fiber Inner diameter ($d_{fibre.in}$)	1.8 mm			
Fiber Outer diameter ($d_{fibre.out}$)	2.7 mm			
Membrane thickness (δ_m)	450 μm			
Shell Inner diameter ($d_{shell.in}$)	20 mm			
Shell Outer diameter ($d_{shell.out}$)	25 mm			

2.2. Model formulation

The following subsections describe the development of the mathematical model employed in this work. First, the governing equations for mass and energy transfer across the membrane are introduced, followed by the formulation of the one-dimensional mass balance for the module. Lastly, the numerical resolution strategy used to solve the coupled system of equations is presented.

2.2.1. Mass and energy transfer through the membrane

Mathematical formulation and model development for DCMD are based on heat and mass transfer principles. As shown in Fig. S2 in Supplementary Material, the process is driven by a temperature difference between a hot feed stream and a colder permeate stream, which creates a vapor pressure gradient. This gradient is the driving force for mass transfer, as water vapor evaporates on the hot side and diffuses through the membrane pores to condense on the cold side. The figure also illustrates a phenomenon known as temperature polarization, which occurs at the membrane-fluid interfaces. The bulk feed temperature is higher than the membrane surface temperature on the feed side due to heat loss through evaporation and conduction. Similarly, the membrane surface on the permeate side is warmer than the bulk permeate stream due to the heat transfer from the feed side. These temperature boundary layers reduce the effective temperature difference across the membrane, decrease the vapor pressure gradient and lowering the mass transfer flux [17,18].

The key equations and correlations used in the modeling are provided below. The mass flux J in DCMD is determined by the equation:

$$J = B\left(P_{f,m} - P_{p,m}\right) \tag{1}$$

where B is the mass transfer coefficient, and $P_{f,m}$ and $P_{p,m}$ are the vapor pressures at the membrane-feed and membrane-permeate surfaces [17]. The vapor pressure can be estimated using the empirical relation:

$$P_{f,m} = exp\left(A - \frac{B}{T_{f,m} + C}\right), \quad P_{p,m} = exp\left(A - \frac{B}{T_{p,m} + C}\right) \tag{2}$$

The calculated Knudsen number in this study is on the order of unity ($Kn \approx 1$). Similar values have been reported in the literature [19]. Since the calculated Knudsen number is close to unity, vapor transport occurs in the transition regime, where both Knudsen diffusion and molecular diffusion contribute to the overall mass transport resistance. In this regime, neither transport mechanism alone is sufficient to describe the vapor transport through the membrane pores. Therefore, the overall mass transfer coefficient is obtained by combining the resistances associated with Knudsen diffusion and molecular diffusion in series, as proposed by [10]. In Eq. (3), the first term inside the brackets represents the resistance due to Knudsen diffusion, which depends primarily on the membrane pore radius, porosity, tortuosity, and the mean membrane temperature. The second term represents the molecular diffusion resistance, which depends on the diffusivity of water vapor in air, the air pressure inside the pores, the total pore pressure, and the membrane structural properties. The reciprocal of the sum of these two resistance terms gives the overall mass transfer coefficient, B, which accounts for the combined contribution of both transport mechanisms in the transition regime.

$$B = \left[\left(\frac{3\tau\delta_m}{2\varepsilon r}\left(\frac{\pi R T_m}{8M}\right)^{\frac{1}{2}}\right) + \frac{\tau\delta_m P_{air} R T_m}{\varepsilon P_{tot} D M}\right]^{-1} \tag{3}$$

where $\tau, \delta_m, \varepsilon, r, R, T_m, M, P_{air}, P_{tot}$ and D denote pore tortuosity factor, membrane porosity, pore radius, universal gas constant, membrane surface temperature, molar mass of water, air pressure, total pressure inside the pore and diffusivity of water vapor, respectively [10]. The membrane surfaces temperatures on feed side $T_{f,m}$ and permeate side $T_{p,m}$ are determined as:

$$T_{f,m} = T_f - \left(T_f - T_p\right)\frac{\frac{1}{h_f}}{\frac{1}{h_v + h_c} + \frac{1}{h_p} + \frac{1}{h_f}} \tag{4}$$

$$sT_{p,m} = T_p + \left(T_f - T_p\right)\frac{\frac{1}{h_p}}{\frac{1}{h_v + h_c} + \frac{1}{h_p} + \frac{1}{h_f}} \tag{5}$$

where T_f is bulk temperature on feed side, T_p is bulk temperature on permeate side, h_c is heat transfer coefficient of the membrane, h_p is permeate side heat transfer coefficient, h_f is feed side heat transfer coefficient, and h_v is vapor heat transfer coefficient [17,18]. These coefficients are given by:

$$h_c = \frac{K_m}{\delta_m} \tag{6}$$

$$h_p = \frac{Nu_p K}{d_e}, \quad h_f = \frac{Nu_f K}{d_e} \tag{7}$$

$$h_v = \frac{J\Delta H_v}{T_{f,m} - T_{p,m}} \tag{8}$$

where K_m, Nu, d_e, K and ΔH_v represent the thermal conductivity of the membrane, Nusselt number, the equivalent diameter, thermal conductivity of water and the latent heat of water vapor, respectively [20]. The Nusselt number for feed and permeate side is determined as [17]:

$$Nu_f = 0.13 Re_f^{0.64} Pr_f^{0.38}, \quad Nu_p = 0.13 Re_p^{0.64} Pr_p^{0.38} \tag{9}$$

where Re and Pr are Reynolds and Prandtl numbers, respectively, to be evaluated at the feed and permeate side. Although the feed and permeate sides have different geometries, the correlation is expressed in terms of Reynolds and Prandtl numbers, which are defined using the respective hydraulic diameters and fluid properties of each side. Therefore, the geometric differences are inherently accounted for,

justifying the use of the same equation for Nusselt number for both sides. Moreover, this correlation demonstrated the best agreement with experimental data in our previous work [17], further supporting its applicability in the present study.

The equivalent diameter refers to the fiber diameter within the solution on the lumen side. In contrast, for the shell-side solution, Equation bellow must be applied because the fibers are arranged in a triangular pattern.

$$d_e = \frac{3.44P_t^2 - \pi d_{fiber,out}^2}{\pi d_{fiber,out}} \tag{10}$$

where P_t is the average distance between centers of the fibers and d_{out} is the outer diameter of fibers.

The latent heat of water vapor (ΔH_v) is calculated by using the following equation:

$$\Delta H_v = 1.7535\left(\frac{T_{f,m} - T_{p,m}}{2} + 2024.3\right) \tag{11}$$

To account for the membrane's porous structure, the tortuosity factor is defined as [17]:

$$\tau = \frac{\varepsilon}{1-(1-\varepsilon)^{1/3}} \tag{12}$$

and the effective thermal conductivity of the membrane is:

$$K_m = K_{polymer}(1-\varepsilon) + K_{air}\varepsilon \tag{13}$$

where $K_{polymer}$ *and* K_{air} represent the thermal conductivities of polymer (membrane material) and air, respectively [17].

2.2.2. One-dimensional mass and energy balances

The one-dimensional model is formulated by applying the conservation of mass and energy to both the feed (tube side) and permeate (shell side) domains along the axial coordinate $z \in [0, L]$ [14,16,21]. Fig. S3 in Supplementary Material illustrates the hollow fiber module in an inside–out configuration (top), together with a schematic of a discrete wall element (bottom), which serves as the control volume for the formulation.

These balances allow the prediction of the local temperatures and velocities of the two streams, denoted as T_f, v_f for the feed and T_p, v_p for the permeate. The fluid properties include density ρ and heat capacity c_p, both assumed uniform at a given axial position. In addition, when the heat transfer relations introduced in the previous section (Eqs. (4)–(8)) are solved simultaneously with the conservation equations, the membrane wall temperatures on both sides ($T_{m,f}, T_{m,p}$) are obtained. In this way, the framework consistently couples the transport of mass (J) and heat (Q) between the two domains, which appear as source terms in the governing equations.

Feed domain:

$$A_{f,T}\frac{\partial(v_f\rho_f)}{\partial z} = -J(t,z)A'_{f,T} \tag{14}$$

$$A_{f,T}\frac{\partial(v_f\rho_f c_{p,f}T_f)}{\partial z} = QA'_{f,T} \tag{15}$$

Permeate domain:

$$-A_{p,T}\frac{\partial(v_p\rho_p)}{\partial z} = J(t,z)A'_{p,T} \tag{16}$$

$$-A_{p,T}\frac{\partial(v_p\rho_p c_{p,p}T_p)}{\partial z} = Q(t,z)A'_{p,T} \tag{17}$$

The governing equations are ordinary differential equations (ODEs) in the axial coordinate, since accumulation and axial diffusion are neglected. This assumption is supported by the large axial Péclet numbers calculated for the operating conditions considered in this study ($Pe \approx 1700$–2200 in the feed channel and 200–5000 in the permeate channel), indicating that convective transport dominates over axial diffusion. To link the balances with the module geometry, the cross-sectional areas and wetted perimeters are respectively described for the feed and permeate by:

$$A_{f,T} = \frac{n_{fibre}\pi}{4}d_{fiber,in}^2 \tag{18}$$

$$A_{p,T} = \frac{\pi}{4}\left(d_{shell,in}^2 - n_{fiber}d_{fiber,out}^2\right) \tag{19}$$

$$A'_{f,T} = n_{fiber}\pi d_{fiber,in} \tag{20}$$

$$A'_{p,T} = n_{fiber}\pi d_{fiber,out} \tag{21}$$

The coupling between the two sides is therefore exclusively represented through the source terms J and Q, which embody the transfer phenomena across the membrane. Radial transport phenomena are not explicitly discretized but represented through the heat- and mass-transfer relations introduced previously. The calculated Graetz numbers ($Gz \approx 40$–0.3 in the feed channel and 1100–0.1 in the permeate channel) support this treatment, as they indicate the expected development of radial temperature profiles along the module. To represent the counter-current configuration, the formulation therefore constitutes a boundary value problem (BVP), with conditions specified such that at $z = 0$ the inlet feed temperature and velocity ($T_{f,in}$,$v_{f,in}$) are known, while at $z = L$ the inlet conditions of the permeate stream ($T_{p,in}, v_{p,in}$) [22,23], as is described in the following equations:

$$T_f(z=0) = T_{f,in} \tag{22}$$

$$v_f(z=0) = v_{f,in} \tag{23}$$

$$T_p(z=L) = T_{p,in} \tag{24}$$

$$v_p(z=L) = v_{p,in} \tag{25}$$

The numerical solution approach for this DCMD model is oriented towards a Differential-Algebraic Equation (DAE) system. To enable efficient computation, the algebraic constraints were reduced in index by Pantelides Algorithm [24], and recasted as Ordinary Differential Equations (ODEs), which allowed the use of the collocation-based MATLAB BVP solver called bvp4c [25].

2.2.3. Optimization procedure

The optimization framework was developed to identify suitable hollow fiber DCMD module configurations under realistic operating conditions. Two module design parameters were selected as decision variables: the contact length (L) and the packing density (ϕ), which defines the internal geometry essentials for mass and energy transference. The packing density is defined as:

$$\phi = \frac{n_{fibre}d_{fiber,out}^2}{d_{shell,in}^2} \tag{26}$$

The operational variability was represented by the inlet temperatures and velocities of the feed and permeate streams, as summarized in Table S2 in Supplementary Material. The optimization procedure was carried out by varying both the design parameters and process input variables within predefined ranges. The contact length (L) was varied from 0.1 to 10 m, while the packing density (ϕ) ranged from 0.10 to 0.80. For the process inputs, the inlet feed temperature $(T_{f,in})$ was varied between 40 and 85 °C, and the inlet permeate temperature $(T_{p,in})$ ranged from 15 to 35 °C. In addition, both the inlet feed velocity $(v_{f,in})$and the inlet permeate velocity $(v_{p,in})$ were considered within the range of 0.025 to 0.125 m/s.

It is worth noting that the inlet velocities are defined as operational inputs. Consequently, the corresponding mass flow rates vary with the available flow area when the packing density changes. In this study, the number of fibers was kept constant, and the packing density was adjusted by modifying the shell diameter. This choice ensures a continuous range of packing densities while preserving an integer number of fibers within the module.

In this way, we attempted to cover a wide range of operational scenarios, limited by eventual temperature as low grade for heating the feed (for example, below 85 °C) and keeping the velocities in frequently used limits to avoid excessive friction loss.

Then, the optimization problem was formulated as a multi-objective minimization targeting two key performance indicators (KPIs) [8]. First, the average permeate flux, it is calculated as the mean across the contact length, which quantifies productivity. Second is the net specific thermal energy consumption (STEC), which accounts for the effective thermal energy required per unit volume of distillate. These KPI are defined as:

$$Flux_{avg} = \frac{1}{A_m}\int_0^L J(z)A_m' dz = \frac{1}{A_m}\sum_{i=1}^{N_{mesh}} \left(J_i\, A_m'\, \Delta z_i\right) \tag{27}$$

$$STEC_{net} = \frac{Q_{in} - Q_{rec}}{\Delta \dot{m}_p} = \frac{A_{f,T}\, v_{f,out}\, c_p \left(T_{f,in} - T_{f,rec}\right)}{A_{p,T}\left(v_{p,out} - v_{p,in}\right)} \tag{28}$$

Cooling energy requirements are not explicitly included in the STEC definition. The permeate inlet temperature is assumed to be maintained at 20 °C, representing a low-temperature stream close to ambient conditions (e.g., tap or cooling water), and therefore readily available.

The strategy considers recovering heat (Q_{rec}) from the outlet permeate flow to exchange with the outlet feed, as shown in Fig. 1. Heat recovery is represented using an ideal counter-current exchanger constrained by a minimum terminal temperature difference of 3 °C. Detailed exchanger design, effectiveness limitations, and hydraulic penalties are not considered, as the objective is to capture recovery potential at a conceptual design level. This distinction emphasizes the role of heat recovery in reducing the effective external energy demand, a critical aspect of the optimization framework.

To ensure robustness, the objectives were evaluated as expected $E(\cdot)$ values across 100 Monte Carlo scenarios, with process inputs sampled from uniform distributions $U(\cdot)$ within their ranges. The problem can thus be written as:

$$\underset{(L,\phi)}{minOF} = \begin{matrix} \left[-E\left(Flux_{avg}\right), E\left(STEC_{net}\right)\right] \\ s.t.\quad \left(T_{f,in}, v_{f,in}, T_{p,in}, v_{p,in}\right) \sim U(\cdot) \end{matrix} \tag{29}$$

Therefor the ranges described in Table S2 are relevant for this work, because the design is based on satisfy as best possible the defined variability.

The number of Monte Carlo realizations was selected based on a statistical convergence analysis. Expected values of flux and net STEC were evaluated using progressively increasing sample sizes up to 10,000 realizations. Relative deviations below 0.5% were observed for both indicators when using 100 realizations compared to the 10,000-sample reference case, indicating that the selected sample size provides sufficiently stable estimates while keeping the computational effort manageable (Supplementary Material, Fig. S5).

Finally, the optimization strategy combined grid exploration, genetic multi-objective algorithms, and ε-constraint scalarization to construct a comprehensive Pareto front [26]. From this set, a compromise solution was selected based on the minimum distance-to-ideal criterion [27], ensuring a balanced trade-off between flux and net STEC.

The selection of an appropriate optimization strategy is important for balancing computational efficiency, solution quality, and interpretability. In this study, the optimization problem involves only two decision variables, namely contact length and packing density, while the objective functions are evaluated through a mechanistic DCMD model coupled with Monte Carlo-based uncertainty analysis. Therefore, a multi-objective optimization approach based on systematic exploration and evolutionary search was selected to provide a robust characterization of the trade-off between permeate flux and net STEC.

Bio-inspired optimization algorithms, including Harris Hawks Optimization, Slime Mould Algorithm, and other nature-inspired approaches, have recently gained attention for solving complex engineering optimization problems due to their strong global search capabilities. For example, Khajavian et al. [28] demonstrated the applicability of bio-inspired algorithms for optimizing membrane bioreactor operation and compared different algorithms, including differential evolution and Harris Hawks Optimization, showing their capability for nonlinear process optimization. However, these approaches are generally more beneficial for problems involving a large number of continuous decision variables, complex constraints, or highly discontinuous search spaces. In the present study, the relatively low dimensionality of the design space allows a more transparent optimization framework where the Pareto solutions can be directly interpreted in terms of module geometry and operating conditions.

Therefore, the selected optimization strategy was considered suitable for the objective of this work, as it enables reliable identification of optimal module configurations while maintaining computational efficiency and providing clear insight into the physical trade-offs governing DCMD energy performance.

3. Results and discussion

This section presents the main results obtained from the developed model, supported by experimental validation and complemented by comprehensive parametric studies and optimization analysis. The discussion is structured to progressively address model reliability, system behavior under varying operating conditions, and the identification of optimal design configurations.

3.1. Model validation

To validate the accuracy and predictive capability of the developed mathematical model, modeled values of flux, feed outlet temperatures, and permeate outlet temperatures were compared with experimental measurements. As shown in Fig. 2, modeled and experimental data exhibit excellent agreement, with all data points closely aligned along the line of parity. The coefficients of determination (R^2) were 0.96 for

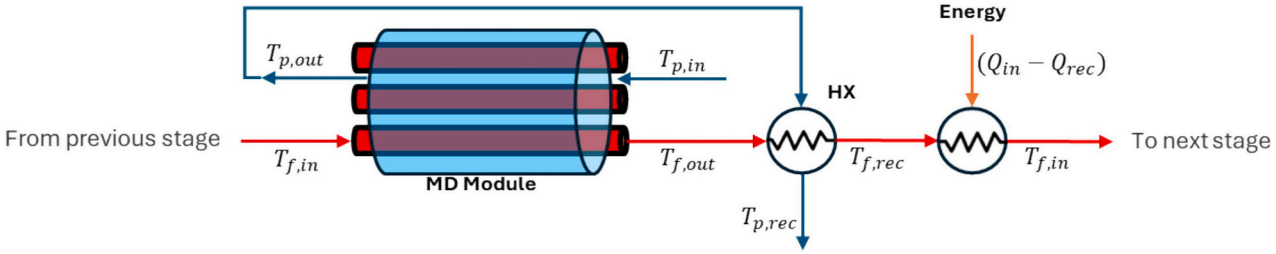


Fig. 1. Energy recovery strategy.

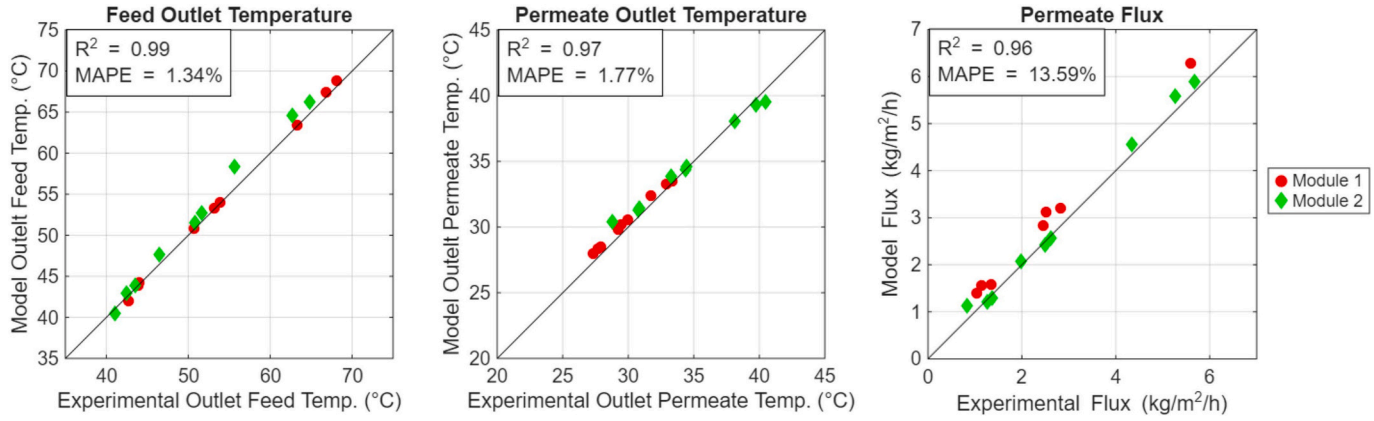


Fig. 2. Comparison of modeled and experimental results for (a) flux, (b) feed outlet temperature, and (c) permeate outlet temperature. The close alignment of data points with the 1:1 line demonstrates excellent model accuracy, with R^2 values exceeding 0.96 for all variables.

flux, 0.99 for feed outlet temperature, and 0.97 for permeate outlet temperature, indicating the model's strong predictive capability. These results confirm that the model accurately represents the coupled heat and mass transfer processes in DCMD and can be confidently applied as a robust and reliable tool for predicting system performance under a wide range of operational conditions.

The Mean Absolute Percent Error (MAPE) was calculated to evaluate the predictive accuracy of the model. The results indicate a MAPE of 13.59% for flux, 1.34% for the feed outlet temperature, and 1.77% for the permeate outlet temperature. It is important to highlight that the model was not calibrated against the present dataset and no model-specific parameter regression was performed. Instead, the model employs established literature correlations to represent the relevant transport phenomena, which supports its general applicability for future use.

The relatively higher error in flux predictions can be attributed to the nature of its measurement, flux is obtained from the slope of a mass accumulation curve over time, which is inherently sensitive to experimental variability. Nevertheless, it is worth noting the coherence of these deviations, which are well balanced between positive and negative errors.

In contrast, the outlet temperature predictions exhibit much lower MAPE values. This reflects the higher stability and reliability of temperature measurements, since the sensors used are less prone to variability and require minimal intervention. Overall, the model demonstrates robust predictive capacity despite the absence of calibration, particularly for temperature-related variables.

3.2. Parametric analysis

The objective of this section is to provide an in-depth analysis of the interplay between operating conditions, module design parameters, and process performance. As a first step, the effect of contact length on key performance indicators is examined at different packing densities under fixed feed and permeate inlet temperatures and velocities, as illustrated in Fig. 3.

As shown in Fig. 3 (a), the feed outlet temperature increases markedly with increasing packing density over the entire range considered. For example, at a contact length of 10 m, the feed outlet temperature rises from approximately 20 °C to 56 °C as the packing density increases from 10% to 80%. In this study, packing density was adjusted by varying the shell diameter. Higher packing densities correspond to smaller shell diameters and, under constant shell-side velocity, require lower permeate flow rates. Consequently, increasing packing density reduces the permeate-to-feed flow rate ratio to approximately 1/10, which decreases the total heat transferred from the feed to the permeate and leads to higher feed outlet temperatures.

An opposite trend is observed on the permeate side (Fig. 3 (b)), where the outlet temperature increases significantly with packing density due to the reduced permeate-to-feed flow-rate ratio. For all packing densities, increasing the contact length results in a decrease in feed outlet temperature and a corresponding increase in permeate outlet temperature, reflecting the longer thermal contact time between the two streams. Fig. 3 (a) and (b) further show that several combinations of packing density and contact length yield permeate outlet temperatures that significantly exceed feed outlet temperatures, indicating favorable conditions for heat recovery from the permeate stream.

The effect of packing density on water flux is shown in Fig. 3 (c), indicating that flux remains largely unaffected up to a packing density of about 40%. Beyond this threshold, a noticeable decline in flux becomes evident as packing density increases further. This trend can primarily be attributed to the difference in relative flow rates of feed and permeate streams under these values of packing densities. Under very low (<20%) packing density conditions, the relative flow rate of the permeate compared to the feed stream becomes very high, up to four times greater. This creates the strongest driving force near the feed entrance of the fiber. However, as the feed contacts the membrane, it rapidly loses heat, which significantly reduces the driving force along the remaining length of the fiber. Thus, later part of the fiber contributes to the vapor transport insignificantly, but total length is still used in the calculation of the flux. With increase in packing density up to 40%, the relative flow rate of permeate keeps on decreasing and reduces the highest driving force that was achieved with low packing densities; however, later portion of the fiber also starts contributing to the flux that results in the similar flux as observed for the low packing densities. With further increase in packing density, the permeate temperature starts approaching the feed temperature after a certain contact length, leading to the observed decrease in average flux. The figure also shows that the decrease is less evident for very small (< 0.3 m) and very long contact lengths (> 5 m). At short contact lengths, feed outlet temperature remains relatively high independent of the feed to permeate flow rates (i.e. packing density), as evident from the figure, and therefore, a high flux is observed independent of the packing density.

We also investigated the effect of packing density on STEC of the system with and without heat recovery. In the case without heat recovery, STEC is calculated according to Eq. 25 but neglecting the recovered heat term. Because the feed outlet temperature decreases with increasing contact length due to greater heat transfer through the membrane, the required heating duty increases, which explains the observed increase in STEC with contact length. For the case of no heat recovery (Fig. 3 (e)), it was observed that the STEC decreases with increasing packing density. This reduction can be attributed to decreasing net heat flux through the membrane with increase in packing densities. As evident from Fig. 3 (c) and (d), although mass flux also

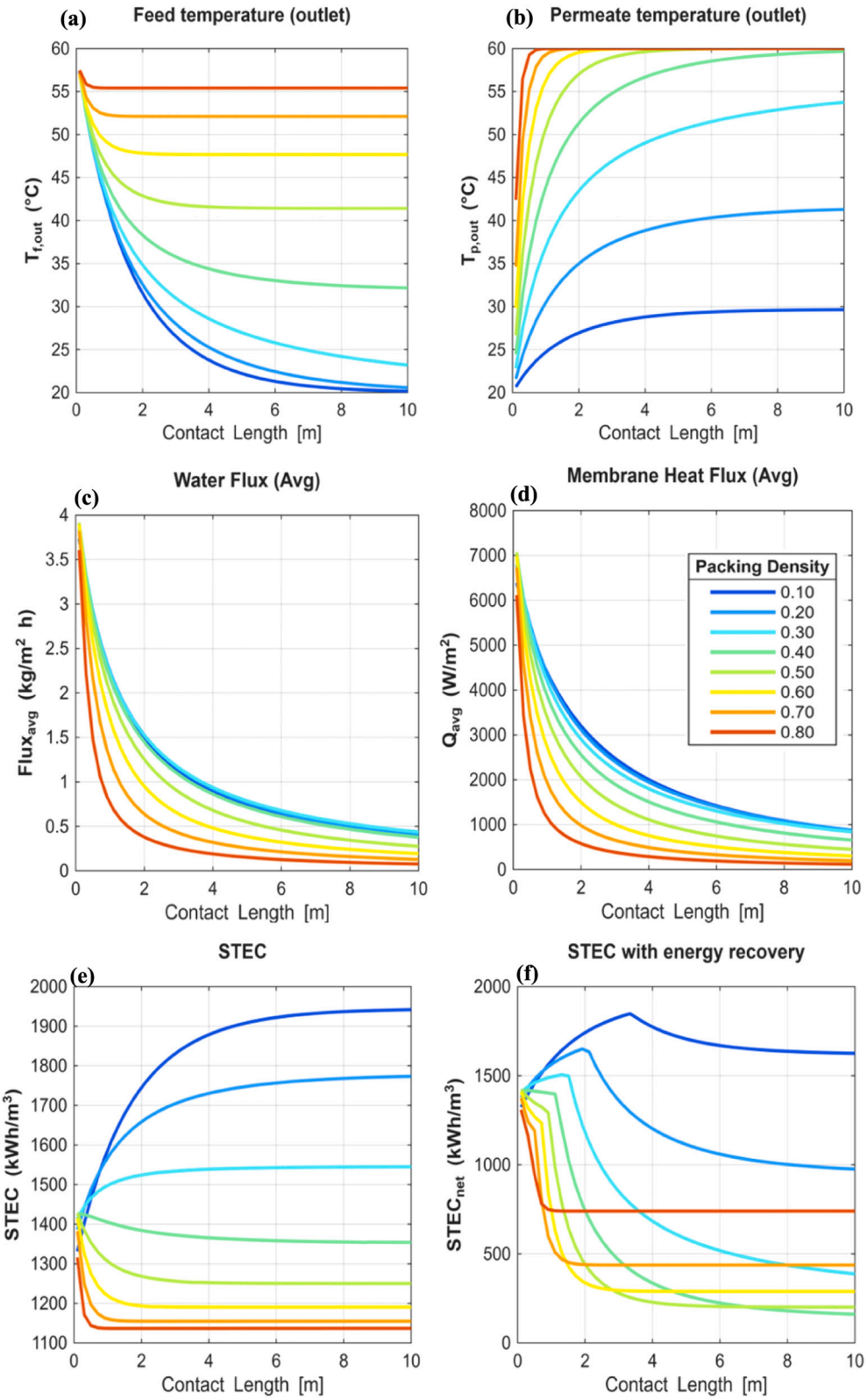


Fig. 3. Effect of contact length on various parameters at different values of packing densities ranging from 0.1 to 0.8. The operating conditions were set at: inlet feed temperature 60 °C, inlet permeate temperature 20 °C, inlet feed velocity 0.125 m/s and inlet permeate velocity 0.025 m/s.

decreases with increase in packing density, a more profound reduction is observed for the total heat flux passing through the membrane. For instance, at contact length of 2 m, the flux decreases by 4.4 times when packing density is increased from 10 to 80% whereas the corresponding heat flux decreases by more than 13 times, leading to the observed decreases in STEC. The decrease in heat flux with increased packing density can be attributed to decrease in conductive heat flux due to increase in permeate temperature that reduces the driving force for the conductive and convective heat transfer across the membrane.

Fig. 3 (f) illustrates the net STEC, calculated as the STEC minus the

recovered heat. Overall, net STEC is strongly influenced by packing density, decreasing by more than a factor of 9 when the packing density is increased from 0.2 to 0.5 at higher contact lengths. As can be seen from the figure, after a certain threshold contact length, net STEC starts decreasing. This threshold corresponds to the point at which heat recovery becomes feasible in the present study, defined by the condition that the permeate outlet temperature exceeds the feed outlet temperature by at least 3 °C. At this point, the permeate stream contains

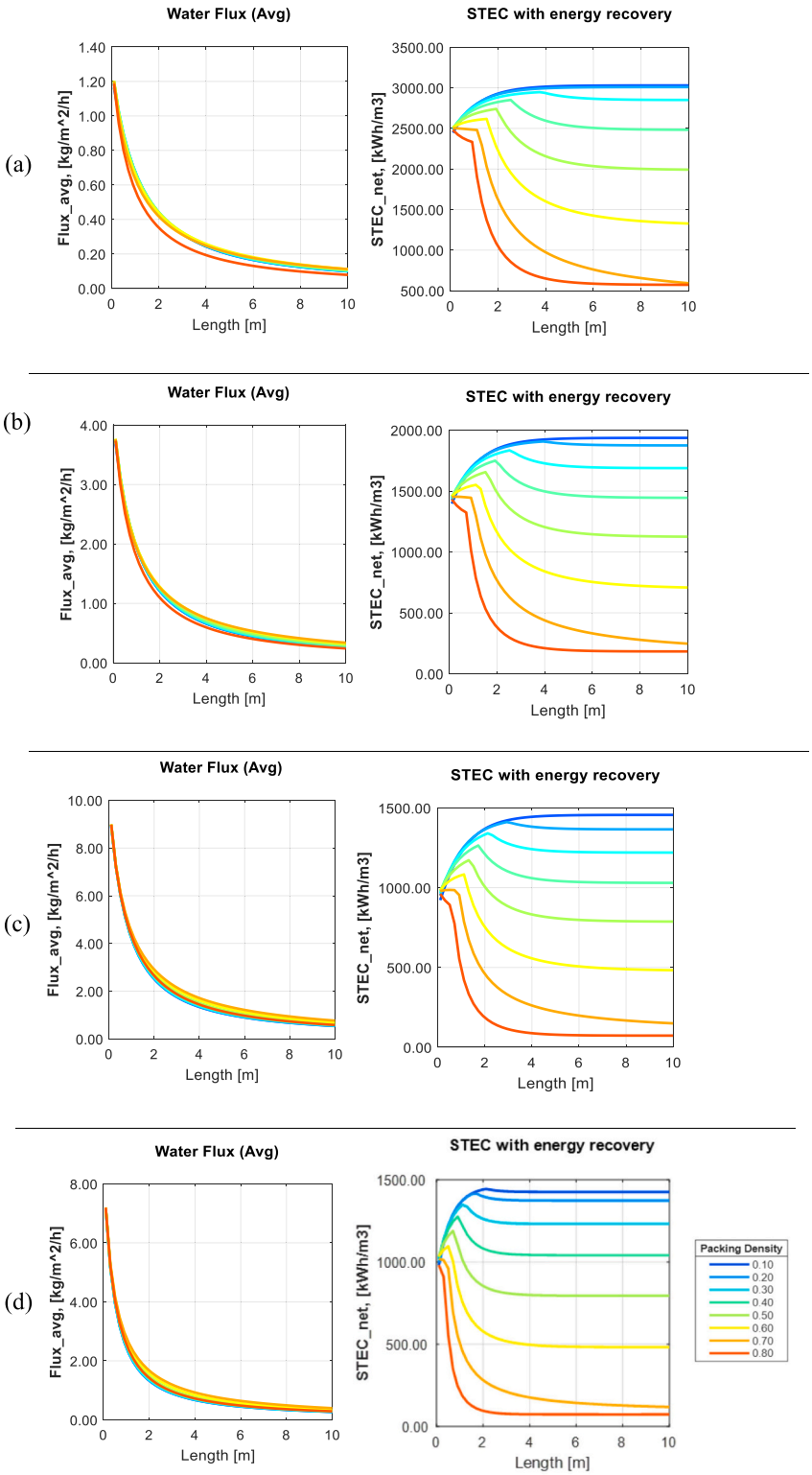


Fig. 4. Effect of contact length on various parameters at different values of packing densities varied from 0.1 to 0.8.
(a) Feed and permeate inlet velocities 0.1 m/s each, feed inlet temperature 40 °C, permeate inlet temperature 25 °C.
(b) Feed and permeate inlet velocities 0.1 m/s each, feed inlet temperature 60 °C, permeate inlet temperature 25 °C.
(c) Feed and permeate inlet velocities 0.1 m/s each, feed inlet temperature 80 °C, permeate inlet temperature 25 °C.
(d) Feed and permeate inlet velocities 0.05 m/s each, feed inlet temperature 80 °C, permeate inlet temperature 25 °C.

sufficient thermal energy to partially preheat the incoming feed, thereby reducing the external heating duty and producing the sharp decrease in net STEC observed in Fig. 3(f). Modules with low packing densities (i.e. with high permeate to feed flow rate ratios) require high contact lengths to satisfy the heat recovery conditions and consequently, the threshold length for these modules switches to high values. It can also be noted that for the lowest packing density considered, the heat recovery potential remains limited due to a high permeate-to-feed flow rate ratio, which prevents the permeate to gain significant temperature for potential heat recovery. As packing density increases, recoverable heat also increases due to a decrease in the permeate to feed flow rate ratio that results in high permeate outlet temperatures compared to the feed outlet temperatures as illustrated in Fig. 3 (a) and (b). However, with packing densities exceeding 40%, STEC starts increasing at long contact lengths. The onset of increase in net STEC shifts to lower contact lengths with increase in packing density. The overall observed increase in net STEC at high (>40%) packing densities is due to a high reduction in permeate flow rate relative to the feed flow rate, which lowers the total recoverable heat content. With decrease in permeate flow rate (i.e. increase in packing density), the flux of the system also keeps decreasing and at certain point, the benefit of increase in heat recovery is surpassed by the decrease in productivity and no further drop in net STEC is observed.

As shown in Fig. 3(a), the feed outlet temperature increases markedly with increasing packing density over the entire range considered. For example, at a contact length of 10 m, the feed outlet temperature increases from approximately 20 °C to 56 °C as the packing density increases from 10% to 80%. In this study, packing density was varied by reducing the shell diameter while maintaining a constant shell-side velocity. Therefore, increasing packing density simultaneously affects the available flow area, permeate flow rate, and membrane area within the module. The reduction in shell diameter decreases the permeate flow cross-sectional area, resulting in a lower permeate flow rate and a reduced permeate heat capacity rate. Consequently, for a given amount of heat transferred across the membrane, the permeate stream experiences a larger temperature increase, while the feed stream retains more thermal energy, leading to a higher feed outlet temperature.

Although increasing packing density also increases the membrane area per module volume and can influence the overall heat and mass transfer characteristics, the observed temperature increase is primarily governed by the change in the permeate-to-feed flow rate ratio. Under the investigated conditions, the permeate-to-feed flow rate ratio decreases from approximately 4 at the lowest packing density to around 0.1 at the highest packing density. This reduction significantly decreases the ability of the permeate stream to absorb heat, resulting in the observed increase in feed outlet temperature. Therefore, the effect of packing density on outlet temperatures is mainly attributed to the change in stream thermal capacity rates rather than membrane area variation alone.

Building on the above analysis of operating conditions and design parameters, further insights are gained by evaluating the influence of module length across a range of packing densities and operative conditions. The idea is to provide an overview of the complex nature of interplay of these design and operational variables on the process performance measured in terms of flux and STEC. Fig. 4 presents simulations for packing densities varying from 0.1 to 0.8 under different operating scenarios: Fig. 4 (a), (b) and (c) at identical feed and permeate inlet velocities of 0.1 m/s with feed temperature of 40, 60, and 80 °C respectively; and Fig. 4 (d), the effect of lower velocities (0.05 m/s) at a feed temperature of 80 °C. In all cases, the permeate inlet temperature is maintained at 25 °C.

It is possible to observe first how sensitive the performance parameters are under the given conditions. The water flux (Fig. 4 (a), top plots) exhibits much stronger sensitivity to contact length, while packing density has a lower influence, as also noted in the previous section. In contrast, the net STEC (Fig. 4 (d), bottom plots) is highly sensitive to both design parameters—contact length and packing density—at all operating conditions. This indicates that contact length is the primary defining factor for flux, whereas energy performance depends on a more balanced interplay of both design variables. These observations are in line with previous findings that highlight the competing influence of module length and hydrodynamic design on transport efficiency [29,30].

Regarding the effect of feed temperature (Fig. 4 (a–c)), the impact on performance is substantial. Higher feed temperatures provide higher maximum fluxes (~1.2, ~3.8, and ~ 7.5 kg h^{-1} m^{-2}, respectively), while also enabling lower maximum STEC values (~3000, ~1900, and ~ 1450 kWh m^{-3}). This behavior is consistent with literature attributing the exponential dependence of flux on feed temperature that exponentially increases the driving force [27,28]. Nevertheless, the extension of contact length shows conflicting trends: flux consistently decreases with length, while STEC initially increases at low packing density but decreases at high packing density due to improved recoverable heat. This type of non-linear response has also been reported for MD systems under varying operating temperatures [31,32].

The effect of feed and permeate velocities is also noteworthy. Reducing velocities from 0.1 to 0.05 m/s at 80 °C (Fig. 4 (c–d)) results in a decrease of maximum flux (from ~10 to ~7 kg h^{-1} m^{-2}). From the perspective of net STEC, the effect on the maximum values is relatively minor; however, the length-dependent trajectories reveal some sensitivity, with inflection points emerging at longer modules. Such velocity-dependent effects are consistent with the reported influence of hydrodynamics on temperature polarization and energy efficiency in MD [30,33,34].

Overall, these results illustrate the strong interdependence between operational conditions and module design. The observed responses are not simple monotonic trends but rather exhibit non-linear behaviours that suggest the existence of intermediate “windows” of operation. Identifying such conditions, where high flux can be achieved alongside low STEC, requires systematic optimization approaches capable of navigating the complex design–operation landscape of membrane distillation.

Additional calculations were performed to assess the impact of hydraulic losses associated with changes in packing density. As expected, increasing packing density led to higher pressure drops due to the reduction in the available flow area. However, the estimated pumping energy remained below approximately 1.5% of the recoverable thermal energy for all evaluated module lengths and packing densities (Fig. S4, Supplementary Material). Therefore, the thermal benefit obtained through heat recovery largely exceeds the additional hydraulic energy requirements, indicating that the observed reductions in net STEC are primarily governed by heat recovery effects rather than by pumping energy consumption.

3.3. Optimal module design

Beyond parametric trends, optimization results are presented to identify the most efficient module configurations. This section details the exploration of design variables and highlights the trade-offs between productivity and energy KPI that define optimal module design and optimal operation conditions.

Fig. 5 provides an overview of the optimization framework and its outcomes. The decision space (Fig. 5(a)) shows the module designs explored in terms of module length (L) and packing density (ϕ), corresponding to a grid of 35 × 35 design combinations. The objective space (Fig. 5(b)) then reports the associated performance indicators, namely the expected permeate flux and the net STEC. For each design point, these KPIs are computed as expected values over 100 Monte Carlo realizations of operational variability (inlet temperatures and velocities, as described in Section 2.2.3). In this sense, each module configuration is evaluated simultaneously across a wide range of operating conditions, ensuring robustness of the reported performance.

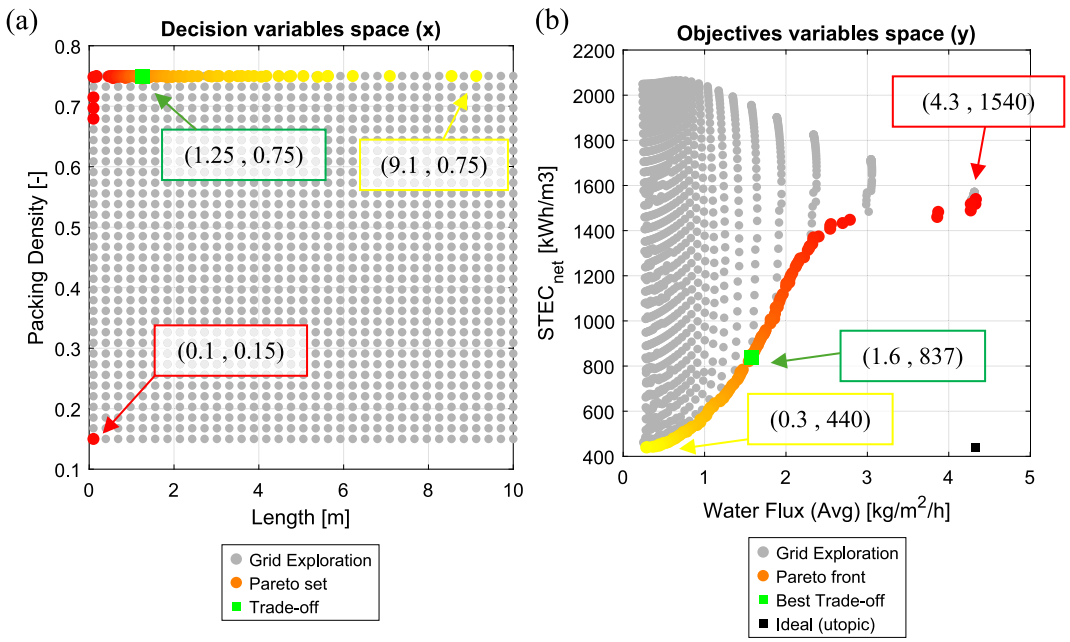


Fig. 5. Results of the initial optimization stage identifying the optimal structural configuration for the DCMD module. In Fig. 5b, each point represents expected/average values over 100 Monte Carlo realization. The optimization, considering length and packing density as decision variables, reveals the pareto front showing the compromise between water flux and net STEC. Three designs are selected for analysis, highlighted in boxes (red, green and yellow), described also in Table 2. (For interpretation of the references to colour in this figure legend, the reader is referred to the web version of this article.)

The grey dots therefore represent the full factorial design space, where each point corresponds to the expected performance of a module configuration under operational uncertainty. Within this feasible region, the conflicting behavior of the two objectives becomes evident, motivating the identification of the non-dominated solutions forming the Pareto front. The black square symbol in Fig. 5(b)) represents the utopian ideal, corresponding to the simultaneous maximization of flux and minimization of STEC, which, as expected, lies outside the feasible region. Building on this initial mapping, the proposed multi-objective strategy identifies the set of non-dominated solutions that form the Pareto front, depicted by the colored markers (yellow to red) in Fig. 5 (b). Notably, this front illustrates the intrinsic trade-off between flux and energy efficiency: any improvement in flux is necessarily accompanied by an increase in STEC, and vice versa. The resulting sigmoidal profile of the Pareto front is consistent with classical patterns reported in multi-objective optimization of separation systems [10,35].

When projected back into the decision space (Fig. 5 (a)), the Pareto set reveals a distinctive distribution: for module lengths greater than approximately 0.2 m, only designs with high packing densities remain competitive, whereas shorter modules are favored only at low packing densities, in coherence with previous research preferring short modules for temperature difference reduction along the module [36], as well larger packing density enhance module performance in productivity [5]. This abrupt shift towards the upper and left boundaries of the design space reflects a transition between two distinct design strategies. Short modules with low packing densities maximize flux by maintaining strong driving forces and limited thermal equilibration, whereas longer modules with high packing densities benefit from enhanced heat recovery and lower net STEC. Intermediate configurations do not provide a sufficient advantage in either objective and therefore become dominated solutions. As a result, the Pareto set concentrates around these two competing design regimes, producing the observed discontinuity in the decision-variable space.

Finally, the green marker in Fig. 5 (b) denotes the compromise solution, identified as the point with the minimum normalized Euclidean distance to the ideal. This design provides a balanced trade-off between flux and STEC, though it should be emphasized that all Pareto-optimal solutions are equally valid depending on the design priorities. In scenarios where energy supply is less restrictive, solutions towards the red end of the front would be preferable, privileging higher flux at the cost of increased energy consumption. Conversely, when energy efficiency is paramount, designs closer to the yellow region would be selected, albeit with reduced productivity.

Table 2 summarizes three representative Pareto-optimal module designs corresponding to distinct operational profiles. The *Low Profile* design is characterized by a very short module length (0.1 m) and low packing density, resulting in high average flux but the highest specific energy consumption (STEC). This configuration favors compactness and productivity per unit area, but at the expense of energy efficiency. In contrast, the *High Profile* design employs a much longer module (9.1 m) with high packing density, leading to substantially lower flux but significantly reduced STEC, and thus improved energy efficiency at the cost of throughput. The *Trade-off* design occupies an intermediate position, balancing flux and STEC through a compact yet high-performance configuration with a length of 1.25 m and a packing density of 0.75.

Although all three configurations are equally optimal in the Pareto sense, the *Trade-off* design provides the most balanced compromise between productivity and energy efficiency under operational variability. When evaluated across the full range of operating conditions, it achieves an expected permeate flux of 1.6 kg m^{-2} h^{-1} with a mean STEC of 837 kWh m^{-3}. This balanced performance, together with its manufacturability and avoidance of excessively long modules or contact lengths that could compromise pressure drop and structural stability, motivates its selection as the reference module design for the subsequent analysis.

3.4. Optimal operation condition

In this study, the trade-off module is first fixed at its optimal design configuration, defined by a module length of 1.25 and a packing density of 0.75. With the geometric and structural parameters constrained to this trade-off optimal design, the focus then shifts to identifying the most optimized operational conditions. Specifically, the effects of inlet

Table 2
Optimal module design.

		Low Profile Optimal Design	Trade-off Optimal Design	High Profile Optimal Design
Design Parameter	Module length (L)	0.1 m	1.25 m	9.1 m
	Packing density (ϕ)	0.15	0.75	0.75
Objectives	E($Flux_{avg}$)	4.3 kg/m^{2}h	1.6 kg/m^{2}h	0.3 kg/m^{2}h
	E($STEC_{net}$)	1540 kWh/m^3	837 kWh/m^3	440 kWh/m^3

E(·) is the mean value for the 100 scenarios under operational variability (Monte Carlo simulations, Eq. (26)).

velocity and inlet temperature are investigated to determine the operating range that yields optimal performance of the defined module.

Under optimal operational conditions (as shown in Fig. 6 and Table 3), the same module demonstrates significantly improved performance. It should be noted that the optimal feed temperature consistently reaches the upper bound of the explored range (~85 °C), indicating that the optimum is constrained by the imposed temperature limit rather than representing an internal optimum within the explored domain.

Regarding the selected conditions along the Pareto front, balanced trade-off point achieves 4.5 kg/m^{2}h at ~200 kWh/m^3, while the low-profile case sustains 2.2 kg/m^{2}h with only 100 kWh/m^3, and the high-profile case pushes flux above 5.5 kg/m^{2}h at 630 kWh/m^3. This operational flexibility highlights the attractiveness of the design for different industrial priorities, allowing for reaching very low STEC values.

Fig. 6 further clarifies the operational drivers behind these outcomes. The Pareto (Fig. 6 (a) and (b)) set indicates that simultaneous increases in feed and permeate velocities are the most correlated inputs with improvements in both flux and energy performance (Fig. 6 (c)), while feed temperature plays a dominant role only at the higher end of the explored range, a trend also observed in literature sensitivity analysis [15]. These insights suggest that optimal operation does not depend solely on extreme temperatures but also on carefully tuned hydrodynamic conditions.

Table S3 in Supplementary Material summarizes representative large-scale and pilot membrane distillation systems reported in the literature, including configurations such as AGMD, VMD and PGMD [37–41]. These configurations typically achieve improved energy efficiency through architectural complexity, such as multi-stage arrangements, internal heat recovery, or enhanced mass and heat transfer pathways. For example, V-MEMD and PGMD systems operate in the range of ~128–255 kWh m^{-3} [37,41], while AGMD systems may reach ~180 kWh m^{-3} or lower depending on heat recovery integration [38], with best-case values near ~105 kWh m^{-3} reported for plate-based configurations with effective energy recovery [40].

In contrast, the present work demonstrates that, under similar conditions, comparable performance levels (~200 kWh m^{-3}) can be achieved within a single-stage DCMD configuration, without introducing additional structural complexity. This suggests that, beyond configuration selection, the interplay between module geometry, hydrodynamics, and thermal management plays a critical role in determining overall system efficiency. In particular, the results indicate that appropriate combinations of contact length and packing density can enhance thermal coupling and enable effective external heat recovery, partially compensating for the absence of internal multi-stage energy reuse.

From a process design perspective, this highlights an alternative pathway for improving MD performance: rather than increasing system complexity, performance gains can be achieved through integrated design and operation optimization.

3.5. Validation of the optimal design

To validate the reliability of the developed model and support the optimization results, additional experiments were conducted using two commercial membrane modules operated under DCMD conditions. As seen in the above section, optimization study predicted that the most

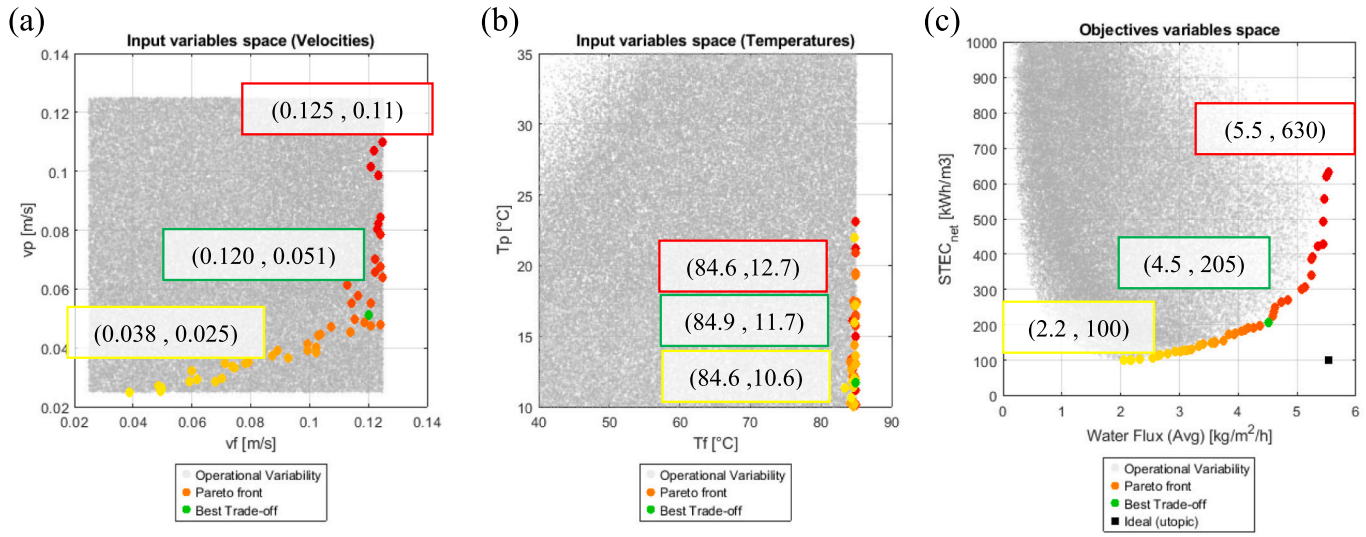


Fig. 6. The optimization identifies the Pareto Front by varying inlet velocities and temperatures to find the optimal operating conditions. **(a)** Input variables (velocities): shows the relationship between the optimal feed velocity ($v_{f,in}$) and permeate velocity ($v_{p,in}$). **(b)** Input variables space (temperatures): shows the relationship between the optimal feed inlet temperature ($T_{f,in}$) and permeate inlet temperature ($T_{p,in}$). **(c)** Objectives variables: The resulting Pareto Front illustrating the trade-off between average water flux and net STEC. Three operational conditions are selected for analysis, highlighted in boxes (red, green and yellow), described also in Table 3. (For interpretation of the references to colour in this figure legend, the reader is referred to the web version of this article.)

Table 3
Optimal operation condition for optimal design at Trade-off Optimal Design (Length = 1.25 and packing density = 0.75).

		Low Profile Condition	Trade-off Condition	High Profile Condition
Operation Condition	Feed temp. $T_{f,in}$	84.6 °C	84.9 °C	84.6 °C
	Permeate temp. $T_{p,in}$	10.6 °C	11.7 °C	12.7 °C
	Feed vel. $v_{f,in}$	0.038 m/s	0.120 m/	0.125 m/s
	Permeate vel. $v_{p,in}$	0.025 m/s	0.051 m/s	0.11 m/s
Objectives	$Flux_{avg}$	2.2 kg/m^{2}h	4.5 kg/m^{2}h	5.5 kg/m^{2}h
	$STEC_{net}$	100 kWh/m^3	205 kWh/m^3	630 kWh/m^3

favorable membrane geometry corresponds to a module packing density of 0.75 and membrane length of 1.25 m, which provides improved thermal performance by enabling the potential partial recovery of heat from the permeate outlet stream for preheating the feed stream. Since fabrication of the exact optimized module was not available at this stage, two experimental modules with similar packing densities (0.73) were tested for model validation. Module 3 had a membrane length of 0.5 m, while Module 4 had a membrane length of 1.0 m. A total of eight experiments were carried out under different operating conditions, including variations in feed inlet temperature, feed/permeate flow rates, and linear velocities, as summarized in Table S1 in Supplementary Material.

The comparison between experimental data and model predictions is presented in Fig. 7 for feed outlet temperature, permeate outlet temperature, and permeate flux. Excellent agreement was obtained between simulated and experimental results. The coefficient of determination (R^2) values were 0.99, 0.98, and 0.96 for feed outlet temperature, permeate outlet temperature, and permeate flux, respectively. In addition, the mean absolute percentage error (MAPE) values were 1.00%, 2.53%, and 6.20%, respectively. In addition, STEC values were calculated to further extend the validation, focusing on Module 4 because its design most closely matches the optimal configuration, obtaining MAPE values of 3% and 7%.

These results confirm that the proposed model accurately predicts the thermal and mass transfer behavior of the DCMD system over a range of operating conditions. Therefore, the model can be considered reliable for optimization studies and for predicting the performance of improved membrane module geometries, including the optimal design identified in this work.

4. Conclusions

This work presented a comprehensive framework for the modeling, simulation, and optimization of hollow fiber direct contact membrane distillation (DCMD) modules, integrating mechanistic model development, experimental validation, parametric analysis, and multi-objective optimization. A one-dimensional model coupling mass and energy balances with membrane transport was developed and solved using a stable and computationally efficient numerical scheme, enabling fast and reliable simulations. Importantly, the model was validated against experimental data with good agreement and without reliance on fitting parameters, ensuring predictive capability and applicability across a wide range of operating conditions.

The parametric analysis provided detailed insight into the individual and combined effects of operating conditions and module design parameters. Beyond confirming expected trends, such as the positive influence of higher inlet temperatures, the results revealed non-intuitive interactions among flow velocities, packing density, and module length. In particular, improvements in permeate flux were not always accompanied by proportional energy penalties, highlighting the importance of jointly considering productivity and energy efficiency when designing DCMD modules.

Building on these insights, a multi-objective optimization framework was applied to maximize permeate flux while minimizing net specific thermal energy consumption (STEC), accounting for operational variability and jointly optimizing module length and packing density. The resulting Pareto front delineated the feasible design space and quantified the intrinsic trade-off between productivity and energy efficiency. A compact and manufacturable optimal design, with a module length of 1.25 m and a packing density of 0.75, was identified. Under operational variability, this design achieved an average flux of 1.6 kg m^{-2} h^{-1} with a mean STEC of 837 kWh m^{-3}, while also exhibiting substantial operational flexibility, reaching energy-efficient conditions of 2.2 kg m^{-2} h^{-1} at approximately 100 kWh m^{-3}.

Overall, these findings demonstrate that DCMD modules, when supported by predictive modeling and uncertainty-aware optimization, can deliver both structural simplicity and operational versatility. The ability to tune operation between energy-efficient and high-productivity regimes, while maintaining manufacturability and design feasibility, underscores the potential of DCMD as a scalable desalination

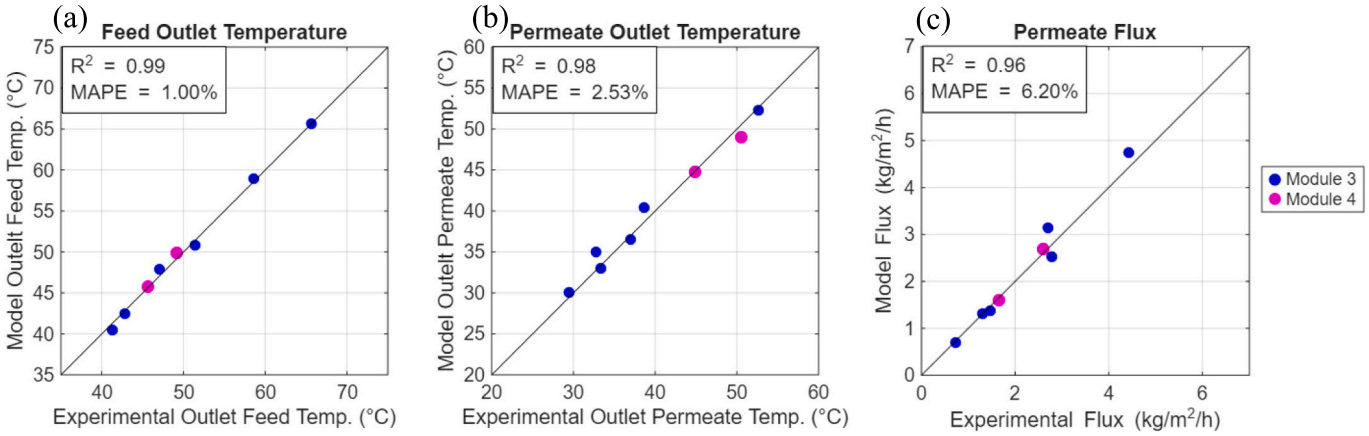


Fig. 7. Experimental validation of the DCMD model using membrane Modules 3 and 4 under different operating conditions: comparison between experimental and predicted values of (a) feed outlet temperature, (b) permeate outlet temperature, and (c) permeate flux. The solid line represents perfect agreement between model predictions and experimental data.

technology, even in applications where more complex configurations such as AGMD or VMD are often considered.

Future work should focus on extending the proposed framework to hybrid and cascade configurations, exploring integration with renewable and waste-heat sources, and validating optimized designs at larger scales. Such efforts would further strengthen the role of DCMD in addressing challenges at the water–energy nexus.

CRediT authorship contribution statement

Hussein Fairousha Sulaiman: Writing – review & editing, Writing – original draft, Validation, Methodology, Investigation, Formal analysis. **Simón Díaz-Quezada:** Writing – review & editing, Writing – original draft, Investigation, Formal analysis, Conceptualization. **Ali Naeimi Tabasian:** Writing – review & editing. **Alberto Tiraferri:** Writing – review & editing. **Cejna Anna Quist-Jensen:** Writing – review & editing, Supervision, Project administration, Methodology, Funding acquisition, Conceptualization. **Aamer Ali:** Writing – review & editing, Writing – original draft, Validation, Supervision, Project administration, Methodology, Investigation, Funding acquisition, Conceptualization.

Declaration of Generative AI and AI-assisted technologies in the writing process

The first complete version of this manuscript was written entirely by the authors. Generative AI (OpenAI's ChatGPT) was used solely to assist in improving clarity, language, and overall presentation. No scientific content, analysis, interpretation, or conclusions were generated by AI. All AI-assisted text was carefully reviewed, revised, and validated by the authors to ensure scientific accuracy and integrity. The authors take full responsibility for the content of the manuscript.

Declaration of competing interest

The authors declare that they have no known competing financial interests or personal relationships that could have appeared to influence the work reported in this paper.

Acknowledgement

The authors acknowledge the financial support of the EU Horizon under the projects MELODIZER "Sustainable membrane distillation for industrial water reuse and decentralised desalination approaching zero waste" (HORIZON-CL4-2022-RESILIENCE-01-14, Grant Agreement No. 101091915) and *CORNERSTONE "Combined technologies for water, energy, and solute recovery from industrial process streams" (HORIZON-CL4-2023-TWIN-TRANSITION-01-40, Grant Agreement No. 101138504)*.

Appendix A. Supplementary data

Supplementary data to this article can be found online at https://doi.org/10.1016/j.jwpe.2026.110673.

Data availability

No data was used for the research described in the article.

References

[1] Water for prosperity and peace, in: UN Water (Ed.), The United Nations World Water Development Report, no. 2024, UNESCO, Paris, 2024.
[2] Y. Soumbati, I. Bouatou, A. Abushaban, Y. Belmabkhout, M.C. Necibi, Review of membrane distillation for desalination applications: Advanced modeling, specific energy consumption, and water production cost, J. Water Process Eng. 71 (Mar. 2025) 107296, https://doi.org/10.1016/j.jwpe.2025.107296.
[3] A.A. Ali, A. Al-Othman, M. Tawalbeh, A. Ali, C.A. Quist-Jensen, M.M.A. Shirazi, Membrane technologies for sustainable development goals: A critical review of bright horizons, J. Environ. Chem. Eng. 13 (1) (Feb. 2025) 114998, https://doi.org/10.1016/j.jece.2024.114998.
[4] I. Hitsov, K.D. Sitter, C. Dotremont, I. Nopens, Economic modelling and model-based process optimization of membrane distillation, Desalination 436 (Jun. 2018) 125–143, https://doi.org/10.1016/j.desal.2018.01.038.
[5] J.-H. Tsai, C. Quist-Jensen, A. Ali, Multipass hollow fiber membrane modules for membrane distillation, Desalination 548 (Feb. 2023) 116239, https://doi.org/10.1016/j.desal.2022.116239.
[6] S. Schilling, H. Glade, Review and analysis of heat transfer in spacer-filled channels of membrane distillation systems, Membranes 13 (10) (Oct. 2023) 842, https://doi.org/10.3390/membranes13100842.
[7] S. Lin, N.Y. Yip, M. Elimelech, Direct contact membrane distillation with heat recovery: Thermodynamic insights from module scale modeling, J. Membr. Sci. 453 (Mar. 2014) 498–515, https://doi.org/10.1016/j.memsci.2013.11.016.
[8] A. Ali, et al., Progress in module design for membrane distillation, Desalination 581 (Jul. 2024) 117584, https://doi.org/10.1016/j.desal.2024.117584.
[9] C. Bustamante, D. Zamora, K. Pérez, E. Troncoso, S. Díaz-Quezada, H. Estay, Optimum hollow fiber air-gap membrane distillation modules: industrial scale design based on performance indicators, Ind. Eng. Chem. Res. 64 (29) (Jul. 2025) 14639–14655, https://doi.org/10.1021/acs.iecr.5c01364.
[10] A. Ali, C.A. Quist-Jensen, F. Macedonio, E. Drioli, Optimization of module length for continuous direct contact membrane distillation process, Chem. Eng. Process. Process Intensif. 110 (Dec. 2016) 188–200, https://doi.org/10.1016/j.cep.2016.10.014.
[11] X. Yang, R. Wang, L. Shi, A.G. Fane, M. Debowski, Performance improvement of PVDF hollow fiber-based membrane distillation process, J. Membr. Sci. 369 (1–2) (2011) 437–447, https://doi.org/10.1016/j.memsci.2010.12.020.
[12] L.-H. Cheng, P.-C. Wu, J. Chen, Modeling and optimization of hollow fiber DCMD module for desalination, J. Membr. Sci. 318 (1–2) (Jun. 2008) 154–166, https://doi.org/10.1016/j.memsci.2008.02.065.
[13] X. Yang, R. Wang, A.G. Fane, Novel designs for improving the performance of hollow fiber membrane distillation modules, J. Membr. Sci. 384 (1–2) (Nov. 2011) 52–62, https://doi.org/10.1016/j.memsci.2011.09.007.
[14] T.-C. Chen, C.-D. Ho, H.-M. Yeh, Theoretical modeling and experimental analysis of direct contact membrane distillation, J. Membr. Sci. 330 (1) (Mar. 2009) 279–287, https://doi.org/10.1016/j.memsci.2008.12.063.
[15] A. Ansari, S. Kavousi, F. Helfer, G. Millar, D.V. Thiel, An improved modelling approach for the comprehensive study of direct contact membrane distillation, Membranes 11 (5) (Apr. 2021) 308, https://doi.org/10.3390/membranes11050308.
[16] L. Martínez-Díez, F.J. Florido-Díaz, M.I. Vázquez-González, Study of polarization phenomena in membrane distillation of aqueous salt solutions, Sep. Sci. Technol. 35 (10) (Jan. 2000) 1485–1501, https://doi.org/10.1081/SS-100100237.
[17] P.M. Hylle, et al., Determination of heat and mass transport correlations for hollow membrane distillation modules, Energies 16 (8) (2023) 3447, https://doi.org/10.3390/en16083447.
[18] M. Khayet, Membranes and theoretical modeling of membrane distillation: A review, Adv. Colloid Interf. Sci. 164 (1–2) (May 2011) 56–88, https://doi.org/10.1016/j.cis.2010.09.005.
[19] N. Cancilla, A. Cipollina, L. Gurreri, M. Ciofalo, Direct contact membrane distillation: a critical review of transmembrane heat and mass transfer models, Membranes 16 (2) (Feb. 2026) 64, https://doi.org/10.3390/membranes16020064.
[20] J.-H. Tsai, et al., Membrane-assisted crystallization: a molecular view of NaCl nucleation and growth, Appl. Sci. 8 (11) (Nov. 2018) 2145, https://doi.org/10.3390/app8112145.
[21] R.W. Schofield, A.G. Fane, C.J.D. Fell, Heat and mass transfer in membrane distillation, J. Membr. Sci. 33 (3) (Oct. 1987) 299–313, https://doi.org/10.1016/S0376-7388(00)80287-2.
[22] M. Momeni, A. Kargari, M. Dadvar, A. Jafari, 3D-CFD simulation of hollow fiber direct contact membrane distillation module: Effect of module and fibers geometries on hydrodynamics, mass, and heat transfer, Desalination 576 (May 2024) 117321, https://doi.org/10.1016/j.desal.2024.117321.
[23] S. Zare, A. Kargari, CFD simulation and optimization of an energy-efficient direct contact membrane distillation (DCMD) desalination system, Chem. Eng. Res. Des. 188 (Dec. 2022) 655–667, https://doi.org/10.1016/j.cherd.2022.10.001.
[24] J.D. Hedengren, T.F. Edgar, Order reduction of large scale DAE models, Comput. Chem. Eng. 29 (10) (Sep. 2005) 2069–2077, https://doi.org/10.1016/j.compchemeng.2005.05.006.
[25] J. Kierzenka, L.F. Shampine, A BVP solver based on residual control and the Maltab PSE, ACM Trans. Math. Softw. 27 (3) (Sep. 2001) 299–316, https://doi.org/10.1145/502800.502801.
[26] S. Chakraborty, S. Chakraborty, A scoping review on the applications of MCDM techniques for parametric optimization of machining processes, Arch. Comput. Methods Eng. 29 (6) (Oct. 2022) 4165–4186, https://doi.org/10.1007/s11831-022-09731-w.
[27] Z. Wang, G.P. Rangaiah, Application and analysis of methods for selecting an optimal solution from the pareto-optimal front obtained by multiobjective optimization, Ind. Eng. Chem. Res. 56 (2) (Jan. 2017) 560–574, https://doi.org/10.1021/acs.iecr.6b03453.
[28] M. Khajavian, J.-M. Lee, S. Lee, M.-H. Hwang, E. Yang, K.-J. Chae, Maximizing nitrogen removal in a membrane bioreactor (MBR) via a swing-basin and dissolved oxygen reduction configuration: a bio-inspired machine learning optimization approach, J. Environ. Chem. Eng. 14 (3) (Jun. 2026) 122535, https://doi.org/10.1016/j.jece.2026.122535.

[29] A. Ali, J.-H. Tsai, K.-L. Tung, E. Drioli, F. Macedonio, Designing and optimization of continuous direct contact membrane distillation process, Desalination 426 (Jan. 2018) 97–107, https://doi.org/10.1016/j.desal.2017.10.041.
[30] H.J. Hwang, K. He, S. Gray, J. Zhang, I.S. Moon, Direct contact membrane distillation (DCMD): experimental study on the commercial PTFE membrane and modeling, J. Membr. Sci. 371 (1–2) (Apr. 2011) 90–98, https://doi.org/10.1016/j.memsci.2011.01.020.
[31] A. Najib, E. Ali, J. Orfi, F.A. Almehmadi, Effect of inlet temperature difference on water production and energy of direct contact membrane distillation for brackish water desalination, Desalination Water Treat. 302 (Aug. 2023) 15–27, https://doi.org/10.5004/dwt.2023.29781.
[32] H.A. Hijaz, M. Zargar, A. Shafieian, A. Razmjou, M. Khiadani, Beyond the surface: understanding temperature polarisation in DCMD membranes through varied operational parameters, Sep. Purif. Technol. 350 (Dec. 2024) 127978, https://doi.org/10.1016/j.seppur.2024.127978.
[33] G. Naidu, S. Jeong, S. Vigneswaran, Influence of feed/permeate velocity on scaling development in a direct contact membrane distillation, Sep. Purif. Technol. 125 (Apr. 2014) 291–300, https://doi.org/10.1016/j.seppur.2014.01.049.
[34] W. Bae, J. Kim, Permeate flux and rejection behavior in submerged direct contact membrane distillation process treating a low-strength synthetic wastewater, Appl. Sci. 10 (2) (Jan. 2020) 677, https://doi.org/10.3390/app10020677.
[35] A.H. Keshavarzzadeh, Design and bio-inspired optimization of direct contact membrane distillation for desalination based on constructal law, Sci. Rep. 10 (1) (Oct. 2020) 16790, https://doi.org/10.1038/s41598-020-73964-7.
[36] A.S. Kim, Cylindrical cell model for direct contact membrane distillation (DCMD) of densely packed hollow fibers, J. Membr. Sci. 455 (Apr. 2014) 168–186, https://doi.org/10.1016/j.memsci.2013.12.067.
[37] A. Najib, et al., An experimental investigation of a solar-driven desalination system based on multi-effect membrane distillation, Desalination Water Treat. 198 (Sep. 2020) 1–18, https://doi.org/10.5004/dwt.2020.26099.
[38] C.-K. Lee, C. Park, Y.C. Woo, J.-S. Choi, J.-O. Kim, A pilot study of spiral-wound air gap membrane distillation process and its energy efficiency analysis, Chemosphere 239 (Jan. 2020) 124696, https://doi.org/10.1016/j.chemosphere.2019.124696.
[39] G. Zaragoza, J.A. Andrés-Mañas, A. Ruiz-Aguirre, Commercial scale membrane distillation for solar desalination, Npj Clean Water 1 (1) (Oct. 2018) 20, https://doi.org/10.1038/s41545-018-0020-z.
[40] D. Woldemariam, A. Kullab, U. Fortkamp, J. Magner, H. Royen, A. Martin, Membrane distillation pilot plant trials with pharmaceutical residues and energy demand analysis, Chem. Eng. J. 306 (Dec. 2016) 471–483, https://doi.org/10.1016/j.cej.2016.07.082.
[41] A. Ruiz-Aguirre, J.A. Andrés-Mañas, J.M. Fernández-Sevilla, G. Zaragoza, Modeling and optimization of a commercial permeate gap spiral wound membrane distillation module for seawater desalination, Desalination 419 (Oct. 2017) 160–168, https://doi.org/10.1016/j.desal.2017.06.019.